Orienting Proteins by Nanostructured Surfaces: Evidences of a Curvature-Driven Geometrical Resonance

Grazia M.L. Messina[1], Gianfranco Bocchinfuso[2], Nicoletta Giamblanco[3], Claudia Mazzuca[2], Antonio Palleschi[2]*, Giovanni Marletta[1]*

[1] Laboratory for Molecular Surfaces and Nanotechnology (LAMSUN), Department of Chemical Sciences, University of Catania, Viale A.Doria 6, 95125 Catania, Italy

[2] Department of Chemical Sciences and Technologies, University of Roma Tor Vergata, Via della Ricerca Scientifica, 00133 Roma, Italy

[3] Institut Européen des Membranes (IEM), Université de Montpellier – 2 Place Eugène Bataillon – 34095 Montpellier cedex - France

ABSTRACT

Experimental and theoretical reports have shown that nanostructured surfaces have a dramatic effect on protein adsorbed amount and conformational state and, in turn, on the performances of the related devices in tissue engineering strategies. Here we report an innovative method to prepare silica-based nanostructured surfaces with a reproducible, well-defined local curvature, consisting in ordered hexagonally packed arrays of curved hemispheres from nanoparticles of different diameter (respectively 147 nm, 235 nm and 403 nm). The nanostructured surfaces have been made chemically homogeneous by partially embedding silica nanoparticles in polyhydroxymethylsiloxane films, further modified by means of UV-O_3 treatments. This paper has been focused on the experimental and theoretical study of laminin, taken as model protein, to study the nanocurvature effects on the protein configuration at nanostructured surfaces. A simple model, based on the interplay of electrostatic interactions between the charged terminal domains of laminin and the nanocurved charged surfaces, closely reproduces the experimental findings. In particular, the model suggests that nanocurvature drives the orientation of rigid proteins by means of a "geometrical resonance" effect, involving the matching of dimensions, charge distribution and spatial arrangement of both adsorbed molecules and adsorbent nanostructures. Overall, the results pave the way to unravel the nanostructured surface effects on intra- and inter-molecular organization processes of proteins.

INTRODUCTION

The proper understanding of cell response to substrate nanotopography, either for natural or synthetic substrates, is mandatory to develop new strategies of regenerative medicine.[1-5] Thus, for instance, micropatterning of surfaces has been shown to be able to determine the cell shape and in turn to influence the growth (and apoptosis) of epithelial cells [1,6] as well as to direct the migration of various mammalian cells.[2,7] Moreover, the nanoscale patterning of biochemical motifs has been shown to determine the cell adhesion and spreading, [8-10] as well as cell differentiation[11,12] and cytoskeletal organization,[13] suggesting a close relationship between the surface nanostructures and the nanosized biochemical machinery that allows cells to respond to environmental stimuli.

The detailed nature of the nanostructure-related factors as well as the mechanism of transmission of the various surface-generated stimuli to cells are still poorly understood, having to account for different factors as the modulation of the intracellular tension,[4,14] the nanoscale clustering of membrane proteins,[8,15] the mechanotransduction of biochemical stimuli,[16] etc… In this framework, local nanocurvature has been suggested to be one of the critical factors influencing the cell behavior on nanostructured surfaces. On the other hand, for a deep understanding of the mediator function between nanotopography and cellular behavior, a clear and detailed picture of the final output, in term of orientation, of the protein adsorption processes is essential. [4, 8-11]

Indeed, a fundamental biological question is still unanswered, i.e., if the cells may detect the nanostructure of the underlying surface by an internal mechanism (e.g., through cytoskeletal strain[6]), or an external one, e.g., involving the sensing of the biochemical or geometric changes in both the membrane or the protein film to which they are attached.

This has produced in recent years a wide debate on the action mechanism of nanotopography on cell behavior. The most obvious approach to study these phenomena has involved the analysis of nanotopography in terms of surface roughness, i.e., a derived parameter accounting for the local structure in an average way, and trying to establish phenomenological relationships between cell behavior and the related average roughness.[17-19]

At variance of this, we think that nanocurvature is one of the key parameters to properly understand the protein configuration/orientation at surfaces.

Indeed, a wide spectrum of surface nanocurvature effects on the adsorbed proteins has been reported in the last few years, ranging from the protein orientation, [20] to the adsorbed protein amount, [21-23] to the conformational state, [24, 25] to the occurrence of aggregation [26-28] or disaggregation [29] processes and to the protein behavior onto curved cell-mimicking membranes.[30,31]

It is worth to mention that the study of the interaction mechanism of proteins with nanostructured surfaces is particularly relevant in the context of tissue regeneration, in view of its application to the understanding of the crucial protein-scaffold and protein-cell membrane interactions.[32-35]

Laminin was chosen as the adsorbing protein, for its rigid and asymmetric shape, suitable to highlight the changes in its arrangement on surfaces upon adsorption, which in turn has been shown to be related to a significant increase of the density, survival rate and network formation of neurons when compared to flat surfaces.[36,37]

In the present paper, we report a combined experimental and theoretical study of the role of nanocurvature, κ, in determining laminin adsorption behavior. The surface topography has been carefully set to rule out any possible interference from competing effects due to chemical inhomogeneity or random distribution of topography. Accordingly, we prepared chemically homogeneous and regularly nanostructured surfaces, consisting in hexagonally packed silica nanoparticle arrays, embedded in a polysiloxane film, finally converted to a silica-like composition by UV-O_3 treatments. Three nanoparticle diameters, respectively 147, 235 and 403 nm have been used, enabling the study of protein adsorption onto nanopatches with well-defined local surface curvature. The obtained nanocurved surfaces have been characterized by means of Atomic Force Microscopy (AFM), while the adsorbed laminin mass and adsorption kinetics have been experimentally measured by means of Quartz Crystal Microbalance with Dissipation monitoring (QCM-D) and the effect of different κ values on the laminin orientation has been investigated by means of FTIR-RAS.

The experimental results have been compared to theoretical simulations results. In particular, in the current theoretical literature the interactions between biomolecules and surfaces have been characterized either by means of atomistic simulations, [38-40] for low-dimensionality, or, when the dimensionality of the system increases, by means of coarse grained [41,42] and mesoscopic model. [43-46] Accordingly, in this paper we have developed an atomistic model for the whole laminin 111 complex, starting from both X-ray data and homology model. The atomistic structure of laminin has been used, in turn, to obtain the structural parameters to build the mesoscopic model used in the Montecarlo simulations of the laminin deposition on the various surfaces. The comparison between experimental and theoretical results has given a clear picture of the main factors playing a role in the nanostructured systems.

EXPERIMENTAL

Laminin

Laminin from Engelbreth-Holm-Swarm murine sarcoma (Mw = 810 000 Da, Sigma-Aldrich, Italy) was used at a concentration of 0.1 μg/ mL in 0.01 mM phosphate buffer solution (PBS, Sigma-Aldrich, Italy) pH 7.4, with 150 mM NaCl.

Nanostructured Substrates

The nanocurved surfaces were built directly on the sensors of a QCM-D apparatus. Hence, the substrates consisted of SiO_2-coated AT-cut quartz crystals. The substrates were cleaned using 10 minutes UV-ozone treatment (Jelight Company, λ_{exc}=185 / 254 nm). The samples were then rinsed by water and dried in a stream of nitrogen.

Aqueous colloidal dispersion of silica nanoparticles, respectively of 403 nm, 235 nm and 147 nm diameter, with hydrophilic anionic surfaces, narrow size distribution, high temperature resistance, and good mechanical stability (from Microparticles GmbH (Germany)) were spin coated on the QCM-D sensor surfaces, yielding a hexagonally close packed array. The spin speed has been adjusted for each class of nanoparticles to obtain homogenously distributed monolayers, whose thickness coincides with the nanoparticle diameter.

Using the nanoparticle arrays as templating systems, a thin film of poly-hydroxymethylsiloxane (Accuglas-T-12B, purchased from Honeywell (USA) and henceforth indicated as PHMS) was employed to embed the nanoparticles, anchoring them each other and to the surfaces, thus preventing possible displacements of the nanoparticles under shear stresses during the QCM-D measurements. The PHMS film was deposited by spin coating solutions at two different dilutions, in a mixture of isopropanol-acetone-ethanol (35-20-45). In particular, a ratio 1:10 was used for 403nm nanoparticles and 1:20 for 235nm and 147nm. The solution concentration and the spin speed were accurately tuned in order to fill the empty spaces among the nanoparticles, avoiding their complete coverage and obtaining regularly nanostructured surfaces of controlled curvature. The curvature, κ, expressed as nm^{-1}, is the inverse of the nanoparticles radius [20] being κ = 0 for the flat reference surfaces.

In particular, the curved portion of nanoparticle emerging from the filling film, for each of the three diameters, has been derived from the section analysis of the AFM images (e.g., figs.1d-f) and used to estimate the global amount of flat and curved areas, under the assumption that the emerging cup has a regular hemispherical shape. More in detail, the curved area per nanoparticle was calculated as follows. At first, the height of the emerging spherical cup, *h,* was calculated by applying simple geometry:

$$h = r - \sqrt{r^2 - a^2}$$

where *r* is the nanoparticle radius and *a* is the radius of the hemispherical cup, obtained from the measured diameter of the emerging part of the nanoparticle after polymer deposition and curing. This allowed, in turn, to calculate the curved area per nanoparticle. The interstitial flat area was calculated as the difference between the surface area of the circle inscribed in a hexagon and the

surface area of the hexagon, as far as the nanoparticles assume an ordered hexagonal close-packed structure. The procedure held a normalizing factor of 3.6.

Atomic Force Microscopy

Atomic Force Microscopy (AFM) measurements were carried out in tapping mode by using a Nanoscope IIIA-MultiMode AFM (Digital Instruments, Santa Barbara, CA, USA). The force was maintained at the lowest possible value by continuously adjusting the set point during the imaging scan. Images were recorded at scan rate of 1 Hz and 512 × 512 pixels per image (i.e., in high resolution conditions) by using 0.5-2 Ω·cm Phosphorous (n) doped silicon tips mounted on cantilevers with a nominal force constant of 40 N/m and a resonant frequency of 300 kHz. Data sets were subjected to a first-order flattening, by using the Veeco NanoScope software, and no further image processing was carried out.

Quartz Crystal Microbalance with Dissipation Monitoring (QCM-D)

The adsorbed amount of Laminin and the adsorption kinetics onto flat and nanostructured surfaces were measured by QCM-D analysis (Q-Sense E1, Biolin Scientific, Sweden). The QCM-D monitors the frequency shifts (ΔF) and the energy dissipation change (ΔD) by applying an oscillatory shear stress obtained by switching off the driving force power periodically. The measurement protocol implied the simultaneous measurement of seven harmonics, i.e., the fundamental frequency of the AT-cut quartz crystal at 5 MHz, and the overtones respectively at 15, 25, 35, 45, 55, and 65 MHz (corresponding to the overtones n = 3, 5, 7, 9, 11, and 13, respectively) was performed.

The protein solutions were pumped into a flow cell containing the quartz crystal using a peristaltic pump at the flow rate 0.150 mL/min. The temperature of cell was maintained at 25 °C.

The frequency shifts for the QCM-D sensors and in turn the adsorbed protein amount, measured for the various nanocurvatures, have been normalized to the a) the active area of the sensors (i.e., 0.2 cm^2), b) the nanoparticle curved area emerging from the embedding polymer layer for each nanoparticle diameter, and c) the area of the interstices among the nanoparticles hexagonally packed.

Finally, due to the very high stiffness of the nanostructured surfaces (i.e., the dissipation change ΔD is lower than $3x10^{-6}$), the laminin adsorbed mass could be calculated by applying the Sauerbrey equation.[47]

FTIR-RAS measurements

Fourier transform infrared reflection-absorption spectroscopy (FTIR-RAS) experiments have been performed by using a Thermo-Scientific (mod. Is50) instrument (Thermo Scientific Inc., Madison, WI, USA), with a Veemax^{TM} III Variable Angle Reflectance Accessory (Pike Technologies, Madison, WI, USA) and a mercury-cadmium-telluride (MCT) detector. Moreover, a polarized incident beam at an incidence angle of 80° with respect to the sample surfaces was used. A total of 516 scans, with a resolution of 2 cm^{-1}, were collected for each sample.

Atomistic model of Laminin 111

The atomistic model of the laminin 111 has been obtained by a hierarchical approach. At first, the structures of the isolated domains were obtained. When the structure of the domain was not available, homology models were built, by using the Swiss Model workspace [48] and the I-Tasser algorithm.[49] The obtained domain structures were then assembled. If possible, the relative arrangement of nearest neighbor domains where obtained by homology with similar multi-domain structures, otherwise the Fread algorithm was used to model the connecting loop regions.[50] The similarity between the domain sequences was evaluated by means of the T-coffe algorithms.[51] The domain charges were evaluated by using the Protein Calculator web tool.[52] The structures were drawn with Chimera.[53]

Montecarlo simulation

The interaction between laminin and the different surfaces was simulated by applying the Montecarlo algorithm to a mesoscale model of the real system. In the model, the surface was considered as perfectly flat or covered with spheres with different diameter. The laminin was considered as a rigid body with the three short arms disposed perpendicularly to the long one, to form an umbrella-like arrangement. The terminal domains were represented as spheres and the joining regions as a sticks. Each laminin was composed by four spheres and four vectors, whose dimensions were singularly evaluated by comparison with the laminin atomistic model. The charges of the spheres were those predicted at neutral pH for the terminal domains. Table 1 summarizes the used parameters for each domain.

Table 1- Model of the laminin complex. Features of the considered beads

Bead Number	Domain	Charge [e]	Radius [nm][a]
1	N-terminal domain (α chain)	+9.9	3.0
2	N-terminal domain β chain)	-5.6	3.0
3	N-terminal domain (γ chain)	-4.1	3.0

4	C-terminal G-like 1 to 5 (α chain)	+ 17.3[b]	6.0

[a] The values are estimated starting from the atomistic model of the complex, by evaluating the radius of the convolution spheres of the corresponding domains.
[b] The charge is calculated on the whole C-terminal region of the α chain, including the interdomain loops

The interaction between the protein domains and the surface was calculated as purely electrostatic, by assuming a coulombian potential in which the distances between the protein beads and the spheres on the surface or the flat surface were considered; an ε equal to 20 and a nominal -1 charge for the surface were used. The interaction between the cohesive regions of the laminin proteins, namely the N-terminal domains of the three chains, represented in the model by the beads 1, 2 and 3, was evaluated in terms of the attractive term in the Lennard Jones equation (equation 1). The segments joining the beads, representing the long and short arms in the laminin complex, were considered as rigid vector with a diameter of 25 nm. The shortest distance between two rods were evaluated according to the reference.[54]

$$V(r) = -\frac{A}{r^6} \qquad (1)$$

In the starting configuration, the laminins were added in a cubic box of 300 nm. During the first $120 \cdot 10^6$ steps of the simulation, the Z dimension, perpendicularly to the surface, was reduced to 100 nm. The configurations sampled during this first steps, were discarded from the ensemble considered for the analyses. Every $4 \cdot 10^6$ steps, an annealing protocols were used, by increasing the temperature until 1000 K in $1 \cdot 10^6$ steps, by keeping this temperature for $1 \cdot 10^6$ steps and then going back to 300 K in $1 \cdot 10^6$ steps. Only the configurations at 300 K were analyzed. Laminin complexes were considered in contact with sphere/surface at distances shorter than 1 nm The number of contacts between the laminins were calculated by considering only the cohesive regions of the protein complex (beads 1, 2 and 3). Two beads were considered in contact when their distance falls below 15 nm. Periodic Boundary Conditions were assumed on the x-y plane.

RESULTS AND DISCUSSION

Preparation and Characterization of substrates with controlled nanocurvature

Figures 1a-c show the Atomic Force Microscopy (AFM) images of the regular hexagonal close-packed 2D structures obtained by using NPs of three different diameters, respectively 147 nm, 235 nm and 403 nm. Both the nominal thickness of the various arrays and the center-to-center distance of neighboring nanoparticles are in agreement with the diameter of the employed NPs and the close-packed arrangement.

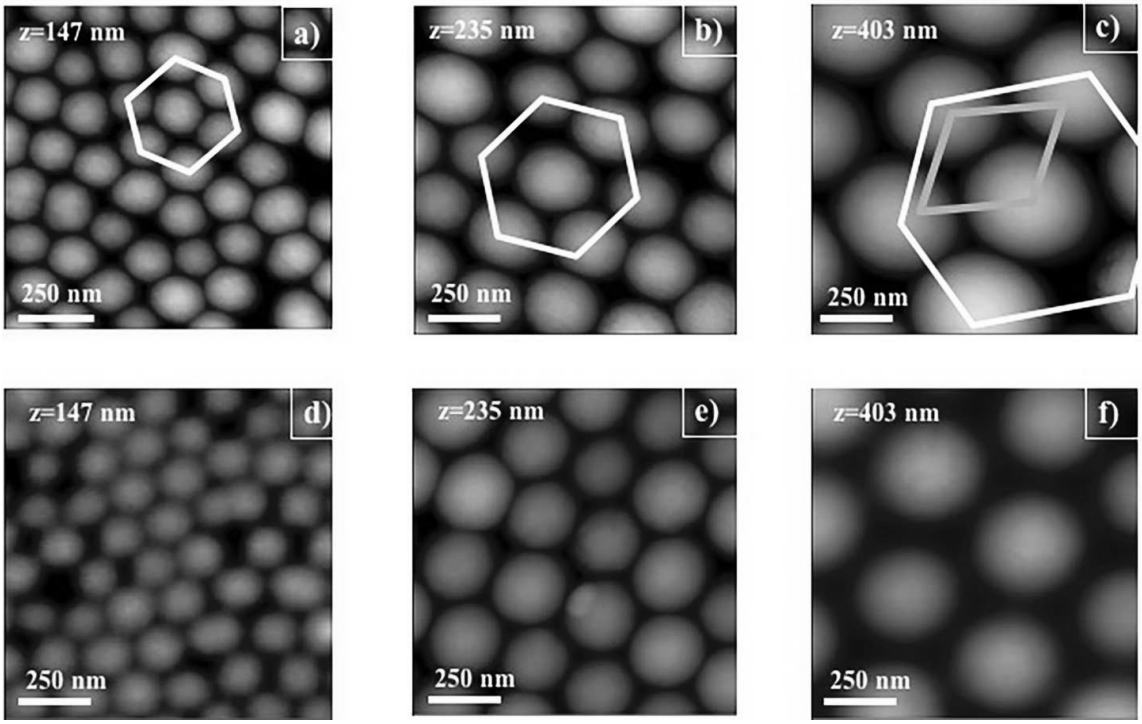

Figure 1- AFM images of arrays of a) 147 nm, b) 235 nm and c) 403 nm free standing SiO_2 NPs; and arrays of d) 147 nm, e) 235 nm and f) 403 nm SiO_2 NPs embedded within PHMS thin film. The hexagonal contours were drawn to drive the eye.

The free standing nanoparticle (NP) arrays have been employed as templating structure to build reproducible and stable nanostructured surfaces with controlled and uniform curvature, by embedding the NP arrays within a spin coated and cured PHMS solution of suitable concentration (see Experimental). To ensure that only the nano-curvature will act as protein configuration driving factor, the methyl-terminated interparticle PHMS areas were converted into $SiO_x(OH)_y$ layers by means of a drastic UV-O_3 treatment, which yielded a uniform chemical composition to the whole nanostructured PHMS/NPs surfaces. The flat substrates have been prepared by spin coating a thin polymer film of PHMS and converting it to a SiO_2-like surface by UV-O_3 treatment. The complete elimination of the methyl groups was confirmed by X-Ray Photoelectron Spectroscopy (data non reported here) and the results are in agreement with previous reports from this Laboratory.[55,56]

Figs. 1d-f report the AFM images for the structure of the final surfaces, showing that the cured PHMS film partially covers the nanoparticles leaving characteristic protruding nanostructures, with convex quasi-hemispherical cups of well-defined dimensions and curvature, and regularly distributed flat areas, in the interstitial spaces among the hexagonally close packed nanoparticles, as shown in Scheme 1. Moreover, section analysis has been performed on the various substrates, finding a similar low-intensity noise, which confirms that the nanoparticle surface roughness, for all the considered samples, is negligible.

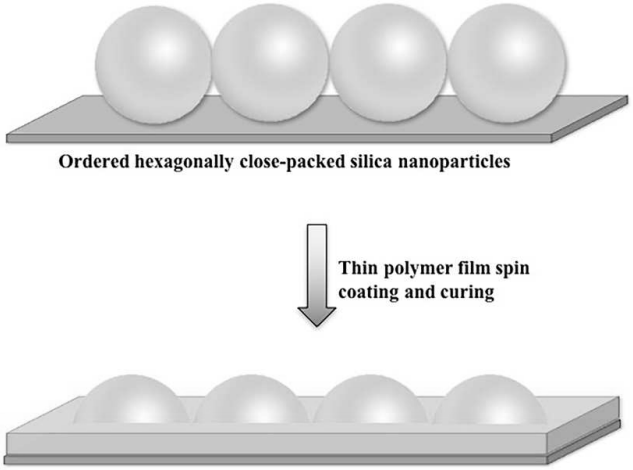

SCHEME 1 – Cartoon of the nanostructured surfaces with controlled-curvature.

In order to rationalize the laminin adsorption process onto the nanostructured surfaces, a detailed analysis of the relative amounts of curved and flat areas has been performed. The nanostructuring process implies, indeed, an increase of the total adsorbing surface, due to the diameter-dependent contribution of the spherical nanoparticles, with an estimated effective area Φ (i.e., the normalized adsorbing area), called, in the following, active area for each type of NP array. This active area has been estimated by normalizing the spherical cup and the interstitial flat area per square micrometer by means the normalizing factor of 3.6 (see Experimental), scaled to the effective sensing area (0.2 cm^2) of the quartz microbalance sensors employed to measure the laminin adsorption. The structural data for the three nanoparticle arrays are reported in Table 2.

Table 2- Curved and flat area percentage, number of nanoparticles/cm^2 and local curvature for the three templating nanoparticles embedded in PHMS ultrathin films.

Nominal nanoparticle diameter	**147 nm**	**235 nm**	**403 nm**
NPs coverage (%)	75.5	65.5	68.7
Hemispherical cups height (nm)	36.0 ± 1.5	81.5 ± 4.5	126.7 ± 2.7
Active area (cm^2), Φ	0.22 ± 0.01	0.34 ± 0.02	0.33 ± 0.01
Curvature (10^{-2} nm^{-1}), κ	1.36	0.85	0.49

Laminin adsorption onto nanocurved surfaces

The adsorption processes have been studied by means of QCM-D technique for each nanostructured surface. The quantitative adsorption data were used to obtain information on the protein organization on the different nanocurvatures.

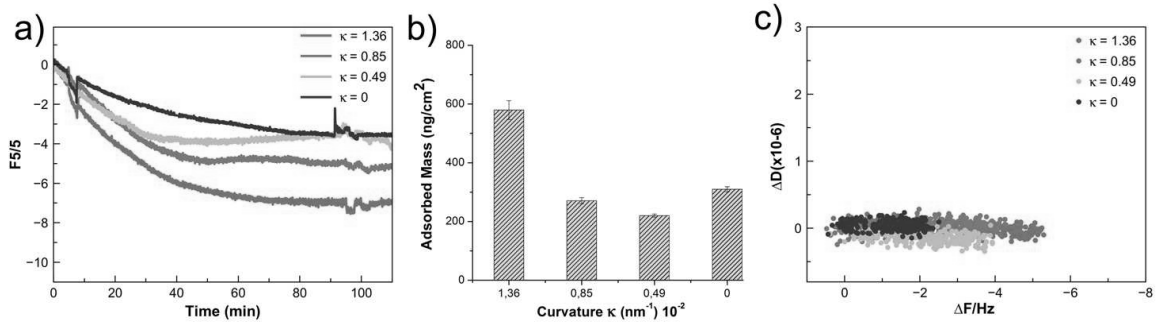

Figure 2 – a) Raw QCM-D traces for laminin adsorption onto surfaces with increasing curvature (the 5th overtone); b) Normalized adsorbed mass depending on active area and local curvature of the substrates; c) corresponding D/F plot for protein adsorption; different colors correspond to the adsorption traces in fig 1a.

Fig. 2a reports the frequency shift (the 5th overtone is reported for simplicity) obtained for the adsorption from a 0.1 μg/ml solution of laminin onto respectively flat and nanostructured surfaces with three different curvatures. It can be seen that the adsorption kinetic is about two-three times faster onto the higher nanocurvature surface (red trace in fig.2a) with respect to the other nanocurvatures and flat surfaces (blue, pale blue and green traces in fig.2a).

Table 3 – QCM-D frequency shifts (ΔF (Hz)), Adsorbed Mass (ng/cm^2) and number of molecules of Laminin adsorbed on different curvature substrates. Raw data are reported as regular type and surface normalized data are reported in bold type.

	ΔF (Hz)	**Mass (ng/cm^2)**	**Molecules/cm^2**
Flat	17.5 ± 0.5	309.7 ± 8.8	$2.3 \cdot 10^{11} \pm 0.7 \cdot 10^{10}$
κ = 1.36 x 10^{-2} nm^{-1} - raw data	-7.2 ± 0.4	127.4 ± 7.1	$9.5 \cdot 10^{10} \pm 5.3 \cdot 10^{9}$
Normalized data (Φ = 0.22)	**-32.72 ± 1.8**	**579.27 ± 32.2**	**$4.3 \cdot 10^{11} \pm 2.4 \cdot 10^{10}$**
κ = 0.85 x 10^{-2} nm^{-1} – raw data	-5.2 ± 0.2	92.4 ± 3.5	$6.8 \cdot 10^{10} \pm 2.6 \cdot 10^{9}$
Normalized data (Φ = 0.34)	**-15.3 ± 0.6**	**270.7 ± 10.4**	**$2.0 \cdot 10^{11} \pm 0.8 \cdot 10^{10}$**
κ = 0.49 x 10^{-2} nm^{-1} – raw data	-4.1 ± 0.1	72.6 ± 1.8	$5.4 \cdot 10^{10} \pm 1.3 \cdot 10^{9}$
Normalized data (Φ = 0.33)	**-12.4 ± 0.3**	**219.9 ± 5.4**	**$1.6 \cdot 10^{11} \pm 0.4 \cdot 10^{10}$**

Fig. 2b and Table 3 summarize the mass adsorbed at equilibrium, evaluated by applying the Sauerbrey equation to the measured frequency shift, according to the very low dissipation of the adsorbed protein layers,[57] and normalized taking into account the active area of the different surfaces (see Table 2). The highest mass uptake, 579.3 ±32.2 ng/cm^2, is found for the surfaces with

the highest local curvature, $\kappa = 1.36x10^{-2}$ (from 147 nm templating NPs), while 270.7 ± 10.4 ng/cm^2 are adsorbed for $\kappa = 0.85\ x10^{-2}$ (from 235 nm NPs) and 219.9±5.4 ng/cm^2 for $\kappa = 0.49\ x10^{-2}$ (from 403 nm NPs) and 309.7 ± 8.8 ng/cm^2 for flat surfaces. Overall, a nanocurvature higher than 1,00 seem to be necessary to observe an increased adsorption with respect to the other nanostructured and flat substrates.

At variance of previously reported results, showing that local chemical and related surface free energy inhomogeneity severely affect the protein adsorption processes[56-59]

Accordingly, the topographical data, reported in Table 2, show clearly that the nanostructured surfaces essentially differ for the local curvature and the active area (i.e., the ratio between curved and flat areas), the highest curvature being related to the lowest active area surface. Hence, by normalizing the results to the active area for each substrate, laminin adsorption results only dependent on the surface curvature at nanoscale (Tables 2 and 3).

Fig. 2c shows the dissipation, D (for the 5th overtone), as a function of the frequency shift of the same overtone, F, for the four surfaces studied here. D/F plots eliminate the explicit time dependence of the adsorption process and highlights the relationship between the amount of adsorbed mass and its viscoelastic behavior (i.e., dissipation), also reflecting, if any, the occurrence of different kinetic steps by slope changes.[60,61] The D/F plots showed an almost null dissipation with increasing mass onto all the substrates, what implies the very high stiffness of the adsorbed layers, and that the adsorption occurs with the same one-step process, i.e., without post-adsorption rearrangements of the adsorbed molecules for all the surfaces.[62]

Summarizing, the experimental adsorption results indicate that the surfaces with the highest curvature, $\kappa = 1.3x10^{-2}$ nm^{-1}, yield a threefold adsorption of laminin with respect to the lower curvature surfaces and twofold with respect to flat surfaces. At the same time, the enhancement of the laminin adsorption occurs only above a nanocurvature threshold, which we can empirically set between $\kappa = 1.3x10^{-2}$ nm^{-1} and $0.85x10^{-2}$ nm^{-1}.

The higher adsorption for $\kappa = 1.3x10^{-2}$ nm^{-1} suggests that on these surfaces laminin molecules are adsorbed with a different orientation with respect to the low curvature and flat surfaces, prompting a different molecular packing.

This last hypothesis has been further investigated by performing FTIR-RAS spectra of the Amide I and II (1800-1400 cm^{-1}) regions of laminin respectively adsorbed onto flat and nanostructured surfaces with the highest curvature value, $\kappa = 1.36\ x\ 10^{-2}$ nm^{-1} (fig.3). Indeed, the analysis of the Amide I bands relative to the C=O stretch in the peptide backbone, [63,64] is diagnostic of the occurrence of preferential oriented adsorption. In the case of peptides in helical conformations, if

the main axis of helices is parallel to the surface, then the transition dipole moment components perpendicular to the helix axis are excited. As a result, the Amide I band gives rise to bands localized roughly at 1650-1660 cm^{-1}. On the contrary, if the main helical axis is perpendicular to the surface, then the transition dipole moment component parallel to it is excited, and the Amide I band shifts to higher wavelengths (roughly 15 cm^{-1}).[65] Figure 3 reports the FTIR spectra of laminin adsorbed on different surfaces. In the spectrum of laminin adsorbed onto the nanostructured surfaces with the highest curvature, the band centered at 1682 cm^{-1} is markedly more intense than in the case of the protein on the flat surface. These data provided a clear information about the orientation adopted by the proteins with respect to the surface indicating that the the presence of sphere with high curvature induces a preferential protein orientation perpendicular to the surface.

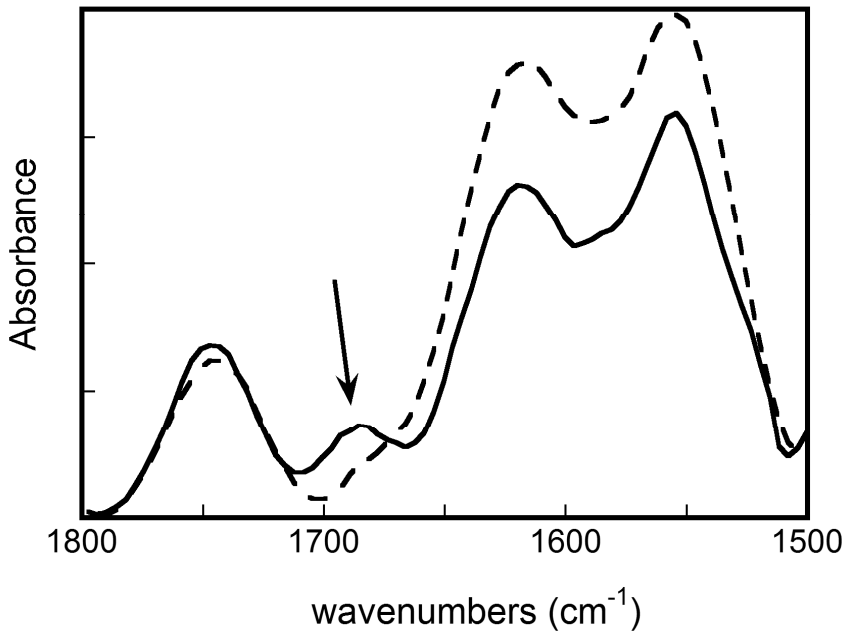

Figure 3 - FTIR-RAS spectra of laminin adsorbed respectively on flat SiO_2 surface (*dashed line*) and nanostructured high curvature surface, $\kappa = 1.36 \times 10^{-2}$ nm^{-1} (*continuous line*). The arrow indicates the band at about 1682 cm^{-1}.

Overall, two peculiar experimental features characterize the laminin adsorption onto nanocurved surfaces: a) the adsorption enhancement, which can be explained in terms of the different way of laminin binding on the surface, as suggested from QCM-D data and confirmed by FTIR-RAS findings, and b) the occurrence of an apparent threshold value in curvature to observe the adsorption enhancement. We propose that this last effect is due to the size matching between adsorbing molecules and nanostructures. This hypothesis has been further investigated by means of theoretical simulations.

Atomistic model of laminin 111

Laminin 111 is a complex formed by 54 different domains (with dimension ranging from tens to hundreds amino acids) and a long tract of triplex structure arranged in a coiled coil motif, constituted by roughly 1700 residues (see fig.4). Only in the case of the β chain, the tract involved in the triple helix is interrupted by a small domain (the α domain), which is 32 residues long. To the best of our knowledge, structures are available for 15 of these domains. These 15 structures cover almost all the domain types present in the laminin 111, except than four domains called laminin IV (A and B type), present in the short arms (two on the α chain and one on both the β and γ chains) and the small α domain presents in the β chain, for which no structural information are available. Starting from the available structures (pdb code: 1klo, 1npe, 1tle, 4aqt, 4aqs and 2jd4) we have built a homology model for 49 domains present in the three chains of laminin 111, by using the Swiss Model workspace. The structure of the remaining domains has been obtained by using the I-Tasser workspace. A tentative structure for the region joining the three chains, which adopts a triple helical conformation, has been obtained starting from a standard coiled coil motif, by using the structure 1swi as a template. The obtained structure measures roughly 80 nm, coherently with the length estimated from AFM images in literature.[66] The great part of the short arms is composed by EGF-like domains (17, 13 and 11 for the α, β and γ chains, respectively). Structures are available with consecutive EGF-like domains; 1klo has been chosen as a template to determine the relative arrangement of nearest neighbor domains. In a similar way, the structure with pdb code 2jd4 has been used to model the relative arrangement of the 5 G-like domains constituting the C-terminal region of the α chain. The remaining lacking loop was modeled by using the Fread algorithm.[50] Figure 4 reports the obtained model of the whole laminin 111, the electrostatic potential and the global charges for the terminal domains are also reported.

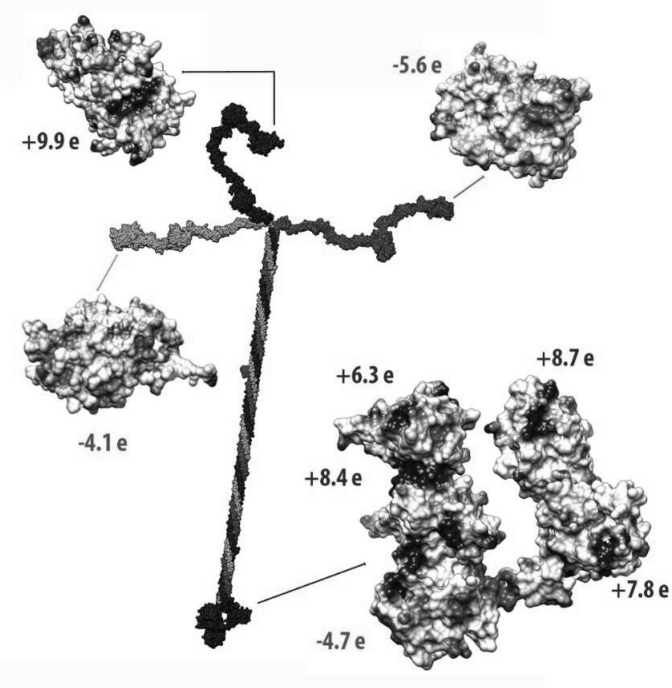

Figure 4 - Putative structure of the murine laminin 111. The α, β and γ chains are colored in blue, red and pink, respectively. The five G-like domains at the C-terminus of the α chain and the N-terminal domains of the α, β and γ chains are reported as solid surfaces colored for the electrostatic potential (-10 Kcal mol^{-1} e^{-1} to +10 Kcal mol^{-1} e^{-1}). For each one of these domains, the total charges are also reported.

Overall, the structural features of the laminin complex are determined mainly by the long triple helical tract, which makes laminin strongly asymmetric and confers a high rigidity to the ternary complex.

Table 4 reports the global charges evaluated at neutral pH for the terminal domains of both human and murine laminin 111. The charge distribution is very similar; in particular, the five C-terminal domains of the α chain show a marked positive net charge, with the exception of the third domain that, in both case, shows a negative charge of -4.7. this similarly suggests a functional role of the charge distribution, which could play a role also in the case here investigated, where the interaction with synthetic surfaces are investigated.

Table 4 - Total charge of the terminal domains in human and murine laminin 111

Domain	Murine	Human
N-terminal (chain α)	+9.9	+7.7
N-terminal (chain β)	-5.6	-5.6
N-terminal (chain κ)	-4.1	-4.1
C-terminal G-like 1 (chain α)	+6.3	+6.5
C-terminal G-like 2 (chain α)	+8.4	+10.1
C-terminal G-like 3 (chain α)	-4.7	-4.7
C-terminal G-like 4 (chain α)	+7.8	+7.8

C-terminal G-like 5 (chain α)	+8.7	+5.2

Montecarlo Model of laminin deposition

To investigate the effect of curvature on the laminin deposition, mesoscale models for the protein and the surfaces were adopted and their interactions has been simulated by applying the Montecarlo algorithm. The goal of these simulations was to individuate which properties are important in these phenomena. An atomistic description of the obtained materials falls out of the scope of these simulations. The laminin molecules were assumed to behave as rigid bodies with the short arms adopting an umbrella like shape. Indeed, the short arms are flexible enough already in the two-dimension space investigated in the AFM experiments,[67] and an umbrella-like form seems the most probable in the formation of an assembly on surfaces,[68] instead of the cross-shape structures associated with the laminin, inferred from the single molecule AFM images[66]. The interaction between surfaces, nanostructured or not, and laminins was simulated with a Coulomb term. The treatment does not consider the effects of the different sphere curvatures on the charge density, which are negligible for SiO_2 spheres with diameter greater than 100nm.[69] The attractive potential between the cohesive regions of the N-terminal domains were described by means of the r^{-6} term of the Lennard-Jones potential; these, moreover, are the only inter-protein attractive interactions considered into the potential function. We cannot exclude the possibility that the electrostatic term could play an important role, as suggested by the similarity between the charges of the N-terminal domains in laminin 111 from different species (see Table 4). However, a simple electrostatic interaction would impair the formation of ternary interactions, experimentally observed during the laminin assembly. Furthermore, experimental studies on the interaction between cohesive regions at different temperature have shown that the process is entropically driven.[68,70] The entropic effects are difficult to reproduce in simple model, like that here adopted, however the aspecific Lennard-Jones interactions between the whole domains (simple spheres in our model) can mime the real conditions better than other specific interaction. The Lennard-Jones attractive constant in the equation 1 (see methods section) and the superficial charge have been assumed to be comparable to each other. To test the influence of the attractive term in the Lennard-Jones potential, two different values, i.e., $2 \cdot 10^6$ and $4 \cdot 10^6$ $kJ \cdot mol^{-1} \cdot nm^6$, for the A parameter in the eq. 1 have been used to simulate the behavior of 15 laminins. When the higher value has been used for the attractive term between the protein domains, a minor tendency to precipitate on the surface has been observed. The results are reported in the Table 5. In the case of simulation with 30 laminin and $B = 2 \cdot 10^6$ $kJ \cdot mol^{-1} \cdot nm^6$ all the proteins interact with the surface/spheres.

Table 5 - Percentage of proteins not in contact with surface/spheres in the simulations with 15 laminins and different A parameter (Equation 1)

Simulations	% of proteins ($A=2\cdot10^6$ kJ·mol^{-1}·nm^6)	% of proteins ($A=4\cdot10^6$ kJ·mol^{-1}·nm^6)
Beads 147 nm	0	20
Beads 235 nm	0	47
Beads 403 nm	0	33
Flat surface	0	27

Figure 5 reports the last frame in the simulation with 15 laminins and A= $2\cdot10^6$ kJ·mol^{-1}·nm^6 in the equation 1. The reported structures are well representative of the acquired ensembles. In the case of spheres with the diameter equal to 147 nm, which are dimensionally comparable with the length of the long arm in the laminin model, interstitial interactions take place between the C-terminal domain of the α chain (positively charged) and the spheres on the surfaces (with a negative charge); indeed, with larger spheres the N-terminal domains of the β and γ chains (negatively charged) would be *forced* too close to the sphere surface.

On the opposite, in the case of spheres with diameter equal to 403 nm, the interstitial deposition is less favorite and the laminins interact mainly with the top surfaces of the spheres. In this case, the larger sphere curvature makes the interactions more similar to those observed for flat surfaces, where many of the positively charged N-terminal domains of the α chain (bead 1 in the model) are in contact with the surface, allowing a double interaction with the surface

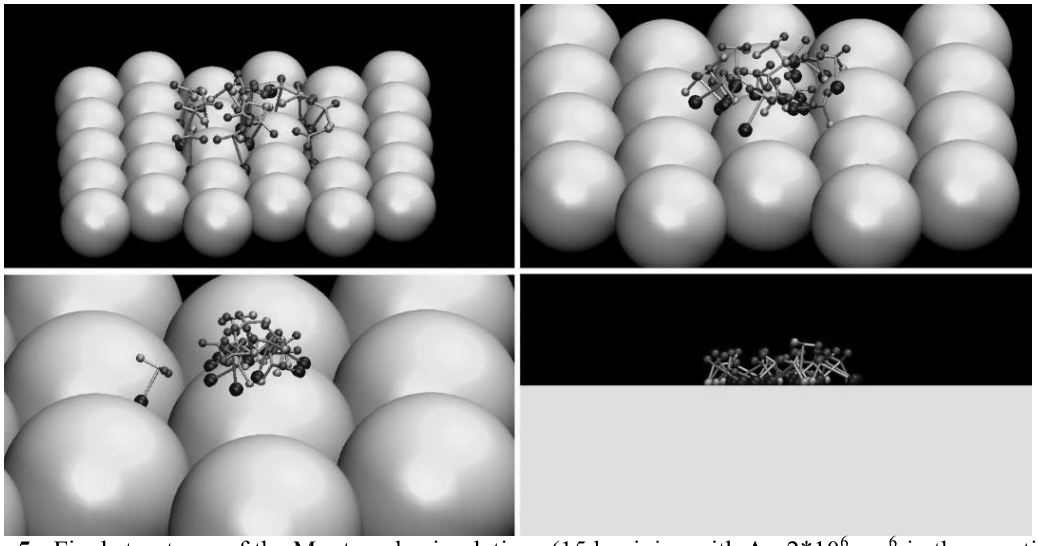

Figure 5 - Final structures of the Montecarlo simulations (15 laminins with A= $2*10^6$ nm^{6,} in the equation 1), of the laminin in the presence of a SiO_2 flat surface (below on the right), a SiO_2 surface covered with SiO_2 NPs with a diameter of 235 nm (above on the right), 147 nm (above on the left), and 403 nm (below on the left). SiO_2 surface and the SiO_2 NPs are colored in yellow. The four arms of the laminin complex are reported as cyan sticks. The beads 2 and 3 (charges of -5.6 e and -4.1 e, respectively) are reported as red

spheres; the bead 1 (charge +9.9 e) is reported as a cyan sphere, and the bead 4, representing all the five G-like domains at the C-terminus of the α chain (charge + 17.3 e) is represented as a bigger blue sphere.

Similarly, with 235 nm diameter spheres, the laminin interact mainly with the top surfaces of the spheres and the interstitial anchoring seems to be less favorite.

To quantitatively evaluate these effects, we have calculated the angle between laminins and surfaces in the ensembles obtained from the simulations performed using different surfaces. Table 6 summarizes these data in the simulations with different conditions. Coherently with the experimental evidences, the spheres with the smallest diameter (147 nm) stabilize the perpendicular arrangement in all the investigated conditions, while the largest spheres (235 and of 403 nm) behave similarly to the flat surface, prompting a "bridging" arrangement. When higher concentration or higher cohesion are simulated increasing the A value, the average angle in the simulations with NPs of 147 nm slight increases; on the contrary, in the other cases a tendency of the angle to decrease is observed.

Table 6 - Average angle between the Z-direction and the long arm of the laminin in the Montecarlo simulations. [a] angles expressed in degree [°]

	15 Laminins[a]		**30 Laminins[a]**
Sphere Diameter (nm)	$A=2\cdot10^6$ kJ·mol^{-1}·nm^6	$A=4\cdot10^6$ kJ·mol^{-1}·nm^6	$A=2\cdot10^6$ kJ·mol^{-1}·nm^6
147	22.7° ± 0.5°	25.3° ± 0.6°	30.0° ± 2.0°
235	50.0° ± 2.0°	23.0° ± 3.0°	39.8° ± 1.5°
403	46.0° ± 3.0°	49.1° ± 0.8°	37.0° ± 2.0°
Flat surface	52.0° ± 6.0°	39.0° ± 0.6°	38.0° ± 2.0°

The number of binary contacts between cohesive regions has been also evaluated (Table 7). These data show that number of contact decrease in the case of surfaces with high curvature, suggesting a major spacing between proteins in these conditions.

Table 7 - Average number of binary contacts between the cohesive domains (beads 1, 2 and 3) in the Montecarlo simulations

	15 Laminins		**30 Laminins**
Sphere Diameter (nm)	$A=2\cdot10^6$ kJ·mol^{-1}·nm^6	$A=4\cdot10^6$ kJ·mol^{-1}·nm^6	$A=2\cdot10^6$ kJ·mol^{-1}·nm^6
147	2.9 ± 1.1	13.0 ± 0.0	9.6±2.1
235	3.0 ± 1.4	14.4 ± 0.7	12.9±2.3
403	3.0 ± 1.2	16.8 ± 0.5	12.0±2.9
Flat surface	5.2±2.5	20.4 ± 1.2	12.6±2.5

"Geometrical resonance" model and laminin deposition

The experimental and theoretical results above reported shed light on the close connection between the nanostructure of surfaces and protein adsorption.

The experiments have been designed to exclude both the possible overlapping effects due to heterogeneous chemical structure of the surface and the multiplicity of structural topographic factors determining the nanostructure of a surface. The study has been focused on the interaction between a protein, characterized by an asymmetric shape and a well-defined charge distribution, and uniformly charged nanostructures, designed to emphasize the role of the curvature of hemispheric nanostructures.

In addition, laminin structure implies a critical relationship between the molecule arrangement on the surface and appropriate epitope exposure or hiding. Furthermore, to neglect the effect of the curvature on the surface charge, NPs with diameter higher than 100 nm have to be used[69]. Laminins, with dimensions in the range of 100 nm allow to study the interaction between rigid proteins and charged nanospheres of comparable dimension, without nanocurvature effects on the charge density.

Thus, the different adsorption for the higher vs. lower curvature surfaces, also according to previous works, [19-29] can be related to changes in the arrangement of the adsorbed molecules, thus depending on the matching of protein and nanostructure geometrical dimensions (see fig.2 above). This hypothesis is supported by the FTIR-RAS results, clearly indicating that a preferential protein orientation, perpendicular to the curved surface, is favored by high curvature.

The Montecarlo calculations showed that a complete and exhaustive picture of the laminin interactions with nanostructured surfaces can be obtained in terms of the interplay of the electrostatic domains on proteins and surfaces and the relevant topographic factors. In particular, at the pH 7.0, both the C- and N-terminals at the α chain, are strongly positively charged, with the charge of the former terminal higher than that of the second one, while the β and γ chain N-terminals are negatively charged and no charged domain is present at the C-terminal in these chains. This fact, taking into account the negatively charged silanol-terminated surfaces, supports the hypothesis that laminin interact with the surfaces predominantly with C- or N-terminal of the α chain. In this case, two arrangements are possible the end-on one, with the C- or N-terminal oriented toward the surface or, in alternative, a "bridging" arrangement, with the C- and N terminal simultaneously linked to the surface and the β and γ chains distant from it.

Accordingly, the most stable arrangement of laminin on the surfaces is found to depend on the β and γ chain terminal distance from the negatively charged surface, in agreement the experimental evidence above discussed. Indeed, the end-on disposition of laminin, with the C-terminal oriented

towards the surface, is strongly stabilized for the high curvature surfaces, due to the matching of the laminin and NP size (i.e., "geometrical resonance" condition). It is to note that the C-terminal end-on arrangement favors the predominant laminin adsorption in the inter-particle interstitial regions, where the electrostatic field is expected to be greater, due to the proximity of nearest neighbor NPs, while on flat and lower curvature NPs, the weighted electrostatic interactions among protein domains (respectively from α, β and γ chains) tend to prompt the "bridging" arrangement favoring the laminin adsorption onto the areas on the top of the hemispherical cups.

These results closely fit the experimental evidence of a critical threshold in nanocurvature, depending on the effective size of the nanocurved structure at the adsorbing surfaces. Accordingly, the theoretical analysis confirms our hypothesis of a necessary geometrical matching between the nanostructure size and the protein dimensions, depending in turn on the spatial arrangement of the charged domains of the proteins with respect to the ones of the nanostructures.

These first results from simulation and the related picture, above proposed, are further supported by the detailed calculation of the angle between the adsorbing laminin axis and the perpendicular to the surface, showing that spheres with the smallest diameter (147 nm) stabilize the perpendicular arrangement in all the investigated conditions, with the average angle between the Z-direction and the long arm of the laminin ranging between 20° and 30° degrees. In this case, with the C-terminal domain of the α chains tightly embedded in the inter-sphere region, a perpendicular-like arrangement locates the negatively charged domains at the N-terminal of the β and γ chains far from the sphere surfaces. On the other hand, for the largest spheres (235 and of 403 nm) average angles between 37° and 50° degrees have been found, very close to values calculated for the flat surfaces. These large values corresponding to the laminin "bridging" arrangement, with the C- and N-terminal anchoring the molecule to the surfaces.

Finally, the analysis of cohesion, simulated by using two values for the A parameter in the attractive term in the Lennard-Jones potential, i.e., $2 \cdot 10^6$ and $4 \cdot 10^6$ $kJ \cdot mol^{-1} \cdot nm^6$, shows that the increase of cohesion induces only a slight increase in the average angle for NPs of 147 nm, while the opposite trend has been found for the low curvature and flat surfaces.

This trend, reinforces the hypothesis that a "bridging" arrangement is indeed favored on the low curvature and flat surfaces. This result provides a further strong support to idea that the orientation of proteins onto nanostructured surfaces mostly depends on a "geometrical resonance" effect, i.e., the occurrence of a critical value of the curvature of the adsorbing nanostructures, in turn determined by the matching of protein and nanostructures, mediated by the fundamentally electrostatic nature of the adsorption-driving interactions.

The described results may account for the differences observed in the dependence on nanoroughness of the adsorption behavior of different size proteins as bovine serum albumin [19,22] (BSA), fibrinogen [43,71] and fibronectin (Fn).[19,22,23,72] It is to note that, as suggested by the D/F plots, no significant difference in the respective adsorption kinetics is observed for the various surfaces, thus confirming that the different adsorption, still occurs as a single-step process, i.e., excluding relaxation processes subsequent to adsorption.

Finally, the proposed "geometrical resonance" is not limited to driving the orientation of molecules with elongated and rigid shapes. Indeed, Tirrell et al. proposed a model predicting that roughness of the same order of the size of macromolecules also increases the deposition of globular macromolecules on such curved surfaces.[73, 74] Of note, in our case the stretching-coiling alternatives for globular end-attached macromolecules, analyzed in the Tirrell model, [73] is replaced by the curvature-driven competition between single end-on and "bridging" attachment. Accordingly, due to the inherent rigidity of the probe laminin molecules, their way of binding to the surface, is driven by nanocurvature and the related geometrical resonance. This finally implies that critical nanocurvature-molecular dimensions matching is required for each specific protein-surface couple.

CONCLUSIONS

The problem of understanding the relationship between geometrical factors, charged domains and packing of proteins at nanostructured surfaces is a foreground research in the field of bioactive surfaces in the last two decades. However, while several experimental and theoretical reports have suggested that relevant reorganization processes, during or after the deposition at nanostructured surfaces, may modify the protein adsorbed amount as well as their packing, less attention has been paid to the inverse problem that is the possibility of controlling the desired exposure of the protein epitopes, by a careful matching of nanostructure geometrical factors and protein dimensions. Indeed, the experimental evidences, in this regards, have been almost exclusively discussed in terms of the nanoroughness, obtaining controversial evidence about the dependence or not of the protein reorganization/reorientation on a given surface.[75] A critical point of this approach is that it is difficult to realize well-constructed surfaces of reproducible nanoroughness. In order to overcome this basic difficulty, in the present work a simple method has been described to prepare silica-based nanostructured surfaces with a well-defined and fully reproducible local curvature and chemically homogeneous nanostructured surfaces. The deposition of laminin, a strongly asymmetric protein, has been studied to highlight the role of the geometrical factors with respect to nanostructuring. Finally, theoretical results demonstrate that the proposed model, mainly based on the role played by electrostatic interactions between the terminal domains of Laminin 111 and the nanocurved

surfaces, is able to closely reproduce the available experimental evidences. The reported results provide an overall picture demonstrating that well-defined charge distributions on the rigid protein molecules and geometrical factors of the surfaces drive the orientation of laminin molecules at surfaces having different nanocurvature.

Summarizing, the curvature effect seems to be tightly linked to the asymmetric nature of the adsorbing molecules. Furthermore, the enhancement or decrease of the deposition involves in turn protein orientation effects, which can be modulated by a "geometrical resonance" between the dimension and spatial arrangement of the adsorbing molecules (i.e., their tertiary and quaternary structures) and nanocurvature.[20, 24-28] Beyond the investigated case, it can be speculated that these arguments have a large validity and as suggested by their analogy with models developed for globular macromolecules end-attached to nanocurved surfaces,[73] as well as for the dependence of protein conformational changes on their relative dimension with respect to the surface roughness.[74,75] Overall, the results here reported pave the way to unravel the world of the nanostructured surface effects on biomacromolecules adsorption and their intra- and inter-molecular organization processes.

Conflicts of interest

"There are no conflicts of interest to declare".

Acknowledgement

G.Marletta gratefully acknowledges the partial financial support of the FIR 2014 programme (University of Catania). G.M.L.Messina acknowledges the financial contribution of Future in Research Programme (MIUR, Italy). A.Palleschi and G.Bocchinfuso acknowledge the financial contribution of the 'Consolidate the Foundation' program (University of Rome Tor Vergata). G.M.L.Messina and G.Bocchinfuso contributed in an equal way to the work.

REFERENCES

1. A. Curtis and C. Wilkinson, *Biomaterials*, 1997, **18**, 1573–1583.
2. C.S. Chen, M. Mrksich, S. Huang, G.M. Whitesides and D.E. Ingber, *Science*, 1997, **276**, 1425–1428.
3. R.G. Flemming, C.J. Murphy, G.A. Abrams, S.L. Goodman and P.F. Nealey, *Biomaterials*, 1999, **20**, 573–588.
4. M.Ventre, F. Causà and P.A. Netti, *J. R. Soc. Interface*, 2012, **9**, 2017–2032
5. C. Fotia, G.M.L. Messina, G. Marletta, N. Baldini and G. Ciapetti, *European Cells and*

Materials, 2013, **26**, 133-149

6. K.A. Kilian, B. Bugarija, B.T. Lahn and M. Mrksich, *Proc. Natl Acad. Sci. USA*, 2010, **107**, 4872–4877.

7. X. Jiang, D.A. Bruzewicz, A.P. Wong, M. Piel and G.M.Whitesides, *Proc. Natl Acad. Sci. USA*, 2005, **102**, 975–978.

8. E.A. Cavalcanti-Adam, T. Volberg, A. Micoulet, H. Kessler, B. Geiger and J.P. Spatz, *Biophys. J.*, 2007, **92**, 2964–2974.

9. M. Arnold, M. Schwieder, J. Blümmel, E.A. Cavalcanti-Adam, M. Lòpez-Garcia, H. Kessler, B. Geiger and J.P. Spatz, *Soft Matter*, 2009, **5**, 72–77.

10. E.A. Cavalcanti-Adam, A. Micoulet, J. Blümmel, J. Auernheimer, H. Kessler and J.P. Spatz, *Eur. J. Cell. Biol.*, 2006, **85**, 219–224.

11. M.J. Dalby, N. Gadegaard, R. Tare, A. Andar, M.O. Riehle, P. Herzyk, C.D. Wilkinson and R.O. Oreffo, *Nat Mater*, 2007, **6**, 997–1003.

12. R.J. McMurray, N. Gadegaard, P.M. Tsimbouri, K.V. Burgess, L.E. McNamara, R. Tare, K. Murawski, E. Kingham, R.O. Oreffo and M.J. Dalby, *Nat Mater*, 2011, **10**, 637–644.

13. L.E. McNamara, T. Sjostrom, K.E. Burgess, J.J. Kim, E. Liu, S. Gordonov, P.V. Moghe, R.M. Meek, R.O. Oreffo, B. Su and M.J. Dalby, *Biomaterials*, 2011, **32**, 7403–7410.

14. P. Tsimbouri, N. Gadegaard, K. Burgess, K. White, P. Reynolds, P. Herzyk, R.O. Oreffo and M.J. Dalby, *J. Cell. Biochem.*, 2014, **115**, 380–390

15. G. Maheshwari, G. Brown, D.A. Lauffenburger, A. Wells and L.G. Griffith, *J. Cell Sci.*, 2000, **113**, 1677–1686.

16. M.J. Dalby, M.J. Biggs, N. Gadegaard, G. Kalna, C.D. Wilkinson and A.S. Curtis, *J. Cell. Biochem.*, 2007, **100**, 326–338.

17. I. Liascukiene, K. El Kirat, M. Beauvais, S.J. Asadauskas, J.F. Lambert ***and*** J. Landoulsi, *Langmuir*, 2017, **33**, 4414–4425,

18. T.F. Keller, J. Schönfelder, J. Reichert, N. Tuccitto, A. Licciardello, G.M.L. Messina, G. Marletta and K.D. Jandt, *Nanoscale*, 2011, **5**, 3120-3131

19. M. Manso Silvàn, G.M.L. Messina, I. Montero, C. Satriano, J.P. Garcìa Ruiz and G. Marletta, *J. Mater. Chem.*, 2009, **19**, 5226-5233.

20. N. Giamblanco, E. Martines and G. Marletta, *Langmuir*, 2013, **29**, 8335–8342.

21. U.B. Jensen, E.E. Ferapontova and D.S. Sutherland, *Langmuir*, 2012, **28**, 11106–11114.

22. P.J. Molino, M.J. Higgins, P.C. Innis, R.M. Kapsa and G.G. Wallace, *Langmuir*, 2012, **28**, 8433-8445.

23. J. Malmstrom, H. Agheli, P. Kingshott and D.S. Sutherland, *Langmuir*, 2007, **23**, 9760-9768.

24. M. Lundqvist, I. Sethson and B.H. Jonsson, *Langmuir*, 2004, **20**, 10639–10647.

25. H.S. Mandal and H.B. Kraatz, *J. Am. Chem. Soc.*, 2007, **129**, 6356–6357.

26. M. Kurylowicz, H. Paulin, J. Mogyoros, M. Giuliani and J.R. Dutcher, *J. R. Soc. Interface*, 2014, **11**, 20130818.

27. M. Kurylowicz, M. Giuliani and J.R. Dutcher, *ACS Nano*, 2012, **6**, 10571–10580.

28. M. Chaibva, K.A. Burke and J. Legleiter, *Biochemistry*, 2014, **53**, 2355–2365.

29. M. Radhakrishna and S.K. Kumar, *Langmuir*, 2014, **30**, 3507-3512.

30. Y. Sugiura, K. Ikeda and M. Nakano, *Langmuir*, 2015, **31**, 11549-11557.

31. W.T. Hsieh, C.J. Hsu, B.R. Capraro, T. Wu, C.M. Chen, S. Yang and T. Baumgart, *Langmuir*, 2012, **28**, 12838–12843.

32. M.M. Stevens and J.H. George, *Science*, 2005, **310**, 1135–1138.

33. L. Ferreira, J. Karp, L. Nobre and R. Langer, *Cell Stem Cell*, 2005, **3**, 136–146.

34. R. Langer and D.A. Tirrell, *Nature*, 2004, **428**, 487–492.

35. M. Dettin, A. Zamuner, M. Roso, A. Gloria, G. Iucci, G.M.L. Messina, U. D'Amora, G. Marletta, M. Modesti, I. Castagliuolo and P. Brun, *PlosOne*, 2015, **10**, e0137505

36. P. Liesi, G. Hager, H.U. Dodt, I. Seppala and W. Zieglgansberger, *J. Neurosci. Res.*, 1995, **40**, 199-206.

37. Y.W. Fan, F.Z. Cui, S.P. Hou, Q.Y. Xu, L.N. Chen and I.S. Lee, *J. Neurosci. Methods*, 2002, **120**, 17-23.

38. R. Latour and L. Hench, *Biomaterials*, 2002, **23**, 4633-4648.

39. J. Feng, J.M. Slocik, M. Sarikaya, R.R. Naik and B.L. Farmer, *Small*, 2012, **8**, 1049-1059.

40. L. Bellucci, G. Bussi, R. Di Felice and S. Corni, *Nanoscale*, 2017, **9**, 2279-2290.

41. R. Li, R. Chen, P. Chen, Y. Wen, P. Ke and S. Cho, *J. Phys. Chem. B*, 2013, **117**, 13451-13456.

42. F. Ding, S. Radic, R. Chen, P. Chen, N. Geitner, J. Brown and P. Ke, *Nanoscale*, 2013, **5**, 9162.

43. K. Rechendorff, M. Hovgaard, M. Foss, V. Zhdanov and F. Besenbacher, *Langmuir*, 2006, **22**, 10885-10888.

44. J. Zhou, H.K. Tsao, Y.J. Sheng and S. Jiang, *J.Chem. Phys*., 2004, **121**, 1050-1057.

45. J. Zhou, S. Chen and S. Jiang, *Langmuir*, 2003, **19**, 3472-3478.

46. C.D. Cooper, N.C. Clementi and L.A. Barba, *J.Chem.Phys.*, 2015, **143**, 09B621_1.

47. G. Sauerbrey, *Zeitschrift Für Phys*., 1959, **55**, 206–222.

48. F. Kiefer, K. Arnold, M. Künzli, L. Bordoli and T. Schwede, *Nucleic Acids Res.*, 2009, **37**, D387-D392.

49. Y. Zhang, *BMC Bioinformatics*, 2008, **9**, 40-47.

50. Y. Choi and C.M. Deane, *Proteins*, 2010, **78**, 1431-1440.

51. C. Notredame, D.G. Higgins and J. Heringa, *J. Mol.Biol.*, 2000, **302**, 205-217.

52. http://protcalc.sourceforge.net/

53. E.F. Pettersen, T.D. Goddard, C.C. Huang, G.S. Couch, D.M. Greenblatt, E.C. Meng and T.E. Ferrin, *J Comput Chem.*, 2004, **25**,1605-1612.

54. C. Vega and S. Lago, *Computer Chem.*, 1994; **18**, 55-59.

55. G. Marletta, S.M. Catalano and S. Pignataro, *Surf. Interf. Anal.*, 1990, **16**, 407-411.

56. C. Satriano, G.M.L. Messina and G. Marletta, *Chem. Comm.*, 2008, **40**, 5031-5033.

57. G.M.L. Messina, C. Passiu, A. Rossi and G. Marletta, *Nanoscale*, 2016, **8**, 16511-16519.

58. M. Rabe, D. Verdes and S. Seeger; *Adv.Colloid Interf.Sci.*, 2011, **162**, 87–106.

59. G.M.L. Messina, C. Satriano and G. Marletta, *Coll.Surf. B*, 2009, **70**, 76-83.

60. M. Rodahl, F. Hook, C. Fredriksson, C.A. Keller, A. Krozer, P. Brzezinski, M. Voinova and B. Kasemo, *Faraday Discuss.*, 1997, **107**, 229-246.

61. I. Reviakine, D. Johannsmann and R.P. Richter, *Anal. Chem.*, 2011, **83**, 8838-8848.

62. P.X. Jia, M. He, Y.K. Gong, X. Chu, J.F. Yang and J. Zhao, *ACS Appl. Mater. Interfaces*, 2015, **7**, 6422-6429.

63. C.R. Cantor and P.R. Schimmel, pp 409-480, in *Biophysical Chemistry, Part 2: Techniques for the Study of Biological Structure and Function*; W.H. Freeman & Company, San Francisco, CA USA 1980.

64. H. Dong, S.E. Paramov and J.D. Hartgerink *JACS*, 2008, **130**, 13691-13695.

65. Y. Miura, S. Kimura, Y. Imanishi and J. Umemura, *Langmuir*, 1999, **15**, 1155-1160.

66. K. Beck, I. Hunter and J. Engel, *FASEB*, 1990, **4**,148-160.

67. C.H. Chen, D.O. Clegg and H.G. Hansma, *Biochemistry*, 1998, **37**, 8262-8267.

68. A. Purvis and E. Hohenester, *J. Biol. Chem.*, 2012, **287**, 44270–44277.

69. M. Barisik, S. Atalay, A. Beskok and S. Qian, *J. Phys. Chem. C*, 2014, **118**, 1836−1842.

70. P.D. Yurchenco and B.L. Patton, *Curr. Pharm. Des.*, 2009, **15**, 1277–1294.

71. H.G. Xie, J.N. Zheng, X.X. Li, X.D. Liu, J. Zhu, F. Wang, W.Y. Xie and X.J. Ma, *Langmuir*, 2010, **26**, 5587–5594.

72. I. Salakhutdinov, P. Van de Vord, O. Palyvoda, H. Matthew, G. Tatagiri, H. Handa, G. Mao, G.W. Auner and G. Newaz, *J. Nanomaterials*, 2008, ID 543170.

73. N. Singh, A. Karim, AF.S. Bates, M. Tirrell and K. Furusawa, *Macromolecules*, 1994, **27**, 2586-2594.

74. A. Dolatshahi-Pirouz, K. Rechendorff, M.B. Hovgaard, M. Foss, J. Chevallier and B. Besenbacher, *Coll.Surf.B*, 2008, **66**, 53-59.

75. M.S. Lord, M. Foss and F. Besenbacher, *Nano Today*, 2010, **5**, 66-78.